Unsupervised Quantum Kernels for One-Class Fault Detection in Industrial Time Series

Kauã Dalla Riva Cucco Barbosa[1], Everson da Silva Flores[1], Bruna de Vargas Guterres[2], Silvia Silva da Costa Botelho[1] and Marcelo Rita Pias[1]

[1]Computer Science Center. Federal University of Rio Grande (FURG), Rio Grande, Brazil
[2]Postgraduate Program on Robotics and Artificial Intelligence, Technological University of Uruguay (UTEC), Rivera, Uruguay
Corresp. author email: kauadallariva@furg.br

***Abstract*—Anomaly detection in industrial time series remains limited by the unavailability of labeled data and weak multivariate fault signatures. This work evaluates whether quantum kernel representations can change anomaly detection behavior under these constraints. A controlled, data-centric benchmarking protocol is defined to isolate the effect of kernel choice in a one-class unsupervised learning setting. The classical OC-SVM and the proposed OC-QSVM are compared under identical preprocessing, dimensionality reduction and optimization conditions across 10 SKAB industrial scenarios, each with 240 nominal training samples. Results show that despite both kernels behaving similarly in direct deviation cases, clear differences emerge in topologically complex scenarios. Reconstruction-based models collapse to degenerate solutions with complete missed detections, whereas kernel methods remain operational. In the most discriminative scenario, the OC-QSVM achieves the highest F1 score (0.733) and maintains bounded error across all cases. Although aggregate performance remains comparable to the classical kernel and exhibits higher false alarm rates, the results suggest that quantum feature spaces can capture multivariate anomaly structure not accessible through single-sensor statistics. These results provide empirical data that quantum kernels alter error distributions in low-data industrial settings and warrant further investigation under real hardware conditions.**

***Index Terms*—Quantum Machine Learning, One-Class SVM, anomaly detection, quantum kernel, industrial time series data and fault detection in the industry.**

I. Introduction

Continuous monitoring of multivariate sensor data is required in industrial cyber-physical systems for predictive maintenance [1]–[5]. Incipient faults are still difficult to detect. They do not reveal as large variations in individual data signals [6], [7]. Instead, they emerge as weak perturbations in multivariate correlations and remain embedded in nominal noise [8]. This condition is further constrained by limited labeled data and class imbalance [9], [10].

Classical anomaly detection methods are widely used [2], [11], but supervised approaches rely on labeled fault data that are often very limited in industrial settings [11], [12]. Unsupervised learning methods are therefore adopted to address this limitation. One-class models and reconstruction-based approaches are used to learn normal behavior [13], [14]. However, limitations are observed in both cases. Kernel-based methods rely on Euclidean distance and may require large datasets to obtain stable boundaries [15], [16]. Reconstruction-based models may fail when anomalies do not shift the learned error distribution. This motivates alternative representations [2], [15].

Quantum machine learning provides a different formulation [17], [18]. Data are mapped into high-dimensional quantum state spaces, in which similarity is evaluated through state overlap [9]. This mapping induces a different geometry in the feature space [19]. In practice, hybrid quantum-classical workflows are adopted, in which preprocessing and optimization are performed using traditional methods. In this case, feature mapping and kernel evaluation are implemented using quantum circuits [20]–[22].

A research challenge remains in the controlled evaluation of quantum kernels for anomaly detection. The existing body of work often compares heterogeneous models or relies on aggregate metrics that do not entirely capture error distributions. The following research question is addressed in this work:
To what extent does replacing a classical RBF kernel with a quantum kernel change the error distribution of one-class anomaly detection under limited training data and varying anomaly structures?

A data-centric benchmarking protocol is defined to isolate the effect of kernel representation. The classical one-class support vector machine (OC-SVM) and the proposed quantum one-class support vector machine (OC-QSVM), both unsupervised learning approaches, are evaluated under identical preprocessing, dimensionality reduction and optimization conditions. This design allows for a controlled comparison in a low-data regime. Validation is performed on the SKAB dataset, which comprises a representative industrial water-circulation system with multivariate sensor data and annotated anomalies [8], [23].

The paper is organized as follows. Section I-A reviews related work. This is followed by Section II, where the classical and quantum models are described. Section III then presents the benchmarking protocol. Section IV reports the experimental results and discussion. Section V concludes the paper.

A. Related Work

Unsupervised anomaly detection has been traditionally based on the One-Class Support Vector Machine (OC-SVM)

TABLE I
SYNTHESIS OF RELATED WORK IN ANOMALY DETECTION

Reference	Algorithm	Dataset	Qubits Feature	Low-data	Metrics (Best)
Schölkopf et al. [24]	OC-SVM (Unsupervised)	USPS Digits	Classical	No	Margin / Visual
Schütt et al. [25]	PAO-ML (Supervised Regression)	Liquid Water	Classical	Yes	Error < 0.1 mHa
Park et al. [26]	VQOCC [QAE] (Semi-supervised)	MNIST, F-MNIST	6–9 qubits	Yes	AUC: 99.9%
Kölle et al. [28]	OC-QSVM [qIT, VS] (One-class)	CC Fraud	2–20 qubits	Yes	AP, F1
Kölle et al. [29]	OC-QSVM + Bagging (One-class)	CC Fraud	2–20 qubits	Yes	AP, F1
Hdaib et al. [27]	QAE + Hybrid Classifiers (Hybrid)	KDD99, IoT-23	–	Yes	–
Badami [2]	QSVM (Supervised)	SWaT, HAI	8 qubits	No	AUC: 99.1%
Cultice et al. [3]	OC-QSVM (One-class)	SWaT, HAI, WADI	8–16 qubits	Yes	F1: 0.95
Tscharke et al. [10]	QSVR (Semi-supervised)	CC, KDD, MNIST	5 features	Yes	AUC: 0.92

[24]. In this approach, a decision boundary is estimated to enclose normal data using kernel mappings. This model defines the reference for kernel-based approaches. Subsequent work has addressed computational and representational constraints. The PAO ML method introduces adaptive bases to reduce cost, although kernel evaluation remains quadratic [25]. This limitation persists across kernel-based extensions and motivates the development of alternative feature representations.

Quantum machine learning has been explored as an alternative. Variational quantum classifiers use quantum encoders and measurement schemes to detect anomalies [26]. Quantum autoencoders have also been used for dimensionality reduction, combined with classifiers such as QSVM and QkNN [27]. In these approaches, the effect of the quantum kernel is not isolated. Evaluations on industrial datasets have been conducted under different assumptions. QSVM was developed and validated on NISQ hardware in a supervised learning setting [2]. Quantum support vector regression was studied under limited data, with performance degradation observed under hardware noise [10]. Methods based on the Quantum Inversion Test reduce kernel computation cost, although sensitivity to noise remains a major shortcoming [28], [29].

Recent work has examined OC-QSVM in industrial environments. Differences in kernel alignment relative to classical functions were reported, which suggest changes in feature space representation [3]. However, controlled comparisons under unsupervised and low-data conditions remain limited.

Table I summarizes the methods, assumptions and limitations across these studies.

B. Contributions

- An unsupervised OC-QSVM is proposed for one-class anomaly detection using a quantum kernel based on the quantum inversion test. The method is integrated into a hybrid quantum-classical workflow in the low-data regime.
- A data-centric benchmarking protocol is defined, where OC-SVM and OC-QSVM are evaluated under reproducible preprocessing, dimensionality reduction and optimization conditions to isolate the effect of kernel representation.
- A controlled comparison is established under 240 nominal training samples across 10 SKAB scenarios, with a factorial design and repeated trials to ensure statistical consistency.
- A scenario-level evaluation is defined using F1 Score, FAR, and MAR to analyze error behavior under direct deviation and topologically complex anomaly structures.
- An empirical assessment is provided showing that OC-QSVM maintains non-degenerate detection and bounded error behavior in complex scenarios, where reconstruction-based models fail.

II. BACKGROUND

Classical machine learning is widely used across application domains, with mature toolchains and stable performance in both supervised and unsupervised learning. However, supervised methods are still constrained by data annotation cost, unbalanced class and domain shift [1], [2], [30]. In contrast, unsupervised approaches are affected by the absence of ground-truth data and sensitivity to noise and parameter selection [1], [8].

A. Hybrid Quantum Classical

In the NISQ regime, gate-based quantum computing is limited by qubit count, coherence time and hardware noise [18]. These constraints restrict fully quantum approaches, leading to hybrid architectures that distribute computation across classical and quantum domains [21]. In this setting, hybrid workflows integrate quantum feature encoding with classical preprocessing and optimization [20]. Quantum kernel methods extend support vector models by mapping data into quantum states and computing similarity through state overlap [18]. Kernel estimation is quantum but the optimization remains classical. Alternative approaches use parameterized circuits, including time series models such as QLSTM [18], [21], [31], or quantum-inspired representations implemented in classical systems [32], [33]. However, these hybrid approaches still incur overhead due to data encoding and classical-quantum interaction [34], [35], and training is affected by barren plateaus [36], [37]. Hardware limitations further constrain scalability and generalization [1], [35].

B. One-Class Support Vector Machine (OC-SVM)

The one-class support vector machine is an unsupervised SVM variant used for anomaly detection [28], [29]. The model is trained using only normal data to estimate a boundary that captures nominal behavior. Deviations are treated as anomalies [3], [27] in this regime. The origin of the coordinate system is associated with the anomalous class, and separation from it is maximized in a high-dimensional feature space [24], [28], [29]. This geometric construction determines the decision

boundary used in the inference. The optimization minimizes the norm of the weight vector w. It allows violations through slack variables ζ_i or ξ_i, controlled by the parameter $\nu \in (0, 1]$, which bounds the fraction of outliers and support vectors [24], [28]. To avoid explicit computation in high-dimensional space, the *kernel trick* is used. Similarity is defined as

$$k(x_i, x_j) = \langle \Phi(x_i), \Phi(x_j) \rangle \tag{1}$$

with common choices including linear, radial basis function (RBF) and polynomial kernels [3]. The model is solved in dual form using Lagrange multipliers. The decision for a new sample is given by

$$\text{Score}(x_{new}) = \sum_{i=1}^{N} \alpha_i \cdot k(x_{new}, x_i) \tag{2}$$

where the sign of the score determines whether the sample lies within the normal region or is classified as anomalous [28], [29].

C. One-Class Quantum Support Vector Machine (OC-QSVM)

The OC-QSVM extends the OC-SVM formulation to a quantum feature space. The model remains unsupervised and is trained solely on normal data without class labels [3], [28]. Samples are initially mapped into a high-dimensional space. A boundary is then estimated to separate the data from the origin of the coordinate system with maximum margin. The decision function is preserved as

$$f(x) = \text{sgn}\left(\sum_i \alpha_i K(x_i, x) - \rho \right) \tag{3}$$

where the kernel K defines the geometry of the boundary [28]. The hyperparameter $\nu \in (0, 1]$ controls the fraction of outliers and support vectors [40]. In this study, $\nu = 0.1$ is used to impose a conservative boundary, consistent with industrial constraints [2].

Quantum Kernel via qIT. The classical kernel is replaced by a quantum kernel based on state fidelity [2], [3]. Similarity is computed in a quantum feature space as

$$K_Q(x_i, x_j) = |\langle \Phi(x_i) | \Phi(x_j) \rangle|^2 \tag{4}$$

This substitution changes the representation of similarity and the resulting decision boundary [2]. The fidelity is estimated using the Quantum Inversion Test (qIT), where $U_\Phi(x_i)$ and $U_\Phi^\dagger(x_j)$ are applied. In this case, similarity is obtained from the probability of measuring the ground state [2], [3], [28]:

$$P(|0 \dots 0\rangle) \tag{5}$$

Dimensionality reduction. PCA, or any other technique, can reduce the input data dimensionality to a smaller number of components, which are mapped one-to-one onto available qubits (in this work, 4 components are mapped to 4 qubits). This configuration limits circuit depth and mitigates noise and decoherence, preserving feasibility under NISQ conditions [2].

Shot noise and regularization. Kernel estimation is stochastic and affected by shot noise, with deviation

$$\sigma \propto \frac{1}{\sqrt{n_{shots}}} \tag{6}$$

This noise may violate the positive semi-definiteness of the kernel matrix and affect the optimization. Tikhonov regularization is applied [38]:

$$K_{reg} = \frac{K + K^T}{2} + \epsilon I \tag{7}$$

with $\epsilon = |\lambda_{min}| + 10^{-6}$, which stabilizes the solution [41].

Key differences between classical and quantum models are summarized in Table II.

D. Classical OC-SVM versus OC-QSVM

Both methods operate under a one-class unsupervised setting, where a boundary is estimated to enclose normal data and separate it from the origin. The main difference lies in how similarity is defined and how the feature space is represented [2], [25], [28]. In the classical OC-SVM, similarity is computed using kernels such as the RBF kernel, based on a defined distance function (e.g., L2 Euclidean). In the OC-QSVM, data are encoded into quantum states and similarity is evaluated through state overlap in Hilbert space [2], [3], [28]. Entangling operations and data-dependent phase rotations are applied within the quantum circuit. Pairwise interactions and nonlinear correlations can be encoded in such a representation. This change in representation also changes how the decision boundary is constructed, particularly under limited data. Differences between the models become more evident in low-data conditions and in the presence of complex structures. Classical methods rely on larger datasets to estimate stable boundaries. In contrast, the OC-QSVM uses a different representation of similarity that may capture multivariate relationships with fewer samples [2], [10]. A structured comparison of these differences is provided in Table II.

III. Methodology

Predictive maintenance in industrial cyber-physical systems relies on continuous sensor monitoring to reduce failures and downtime [1], [2]. Although abrupt faults can be detected by threshold-based rules, detection of incipient faults remains a challenge in Industry 4.0 and 5.0 settings [42], [43]. Such faults do not clearly appear in a single sensor signal. They tend to emerge as weak changes in multivariate correlations and remain embedded in nominal noise [8]. The problem is constrained by class imbalance, since anomaly data are scarce and very difficult to label [9], [10]. Unsupervised models are therefore used, but they often fail to separate noise from early degradation, leading to high missed and false-alarm rates [2]. Quantum kernel methods have been examined as an alternative in which data are mapped into high-dimensional quantum state spaces to define decision boundaries [9].

TABLE II
OC-SVM (RBF KERNEL) VS. OC-QSVM (QIT KERNEL)

Characteristic	Classical OC-SVM (RBF Kernel)	Quantum OC-QSVM (qIT Kernel)
Representation Space	Data are projected into a continuous space of infinite dimension under a Euclidean metric [24].	Data are encoded into pure states within an exponential Hilbert space. The representation is defined by quantum state preparation [28].
Similarity Metric	Similarity is computed analytically through a radial distance function [10], [28].	Similarity is estimated through quantum fidelity. State overlap is measured using the Quantum Inversion Test [28], [29].
Performance under Low Data	A large number of normal samples is required to define a stable decision boundary [2].	Generalization is achieved with a limited number of samples. Latent structures are captured through the geometry of the Hilbert space [2].
Matrix Stability	The kernel matrix is analytically positive semi-definite. Convex optimization is preserved [24].	The matrix is stochastic and affected by shot noise. Regularization based on the Tikhonov method is required [38].
Dimensional Dependence in NISQ	High-dimensional feature sets are handled without major computational constraints [2].	Gate noise limits the effective dimension in current hardware. Dimensionality reduction is required prior to encoding [2].
Time Complexity	Quadratic complexity $\mathcal{O}(n^2)$ is observed with respect to the training set size [39].	Quadratic scaling is intrinsic. Linear scaling $\mathcal{O}(n)$ can be obtained when combined with variable subsampling [12].

A. Dataset: Skoltech Anomaly Benchmark (SKAB)

The SKAB is used as the evaluation dataset [23]. It represents an industrial water circulation system composed of interconnected components, including valves, pumps and rotating elements such as rotors. The system is monitored by sensors that generate multivariate time series comprising accelerometer, pressure, temperature, voltage, current and flow-rate measurements. Ground truth anomaly labels are available. The dataset contains more than 42,000 samples over 1,140 minutes and includes multiple fault scenarios [8]. In this work, 10 scenarios are selected, each with 300 samples. This leads to 3000 samples for controlled comparison.

B. Experimental Batch and Scenario Structure

A subset of data files (D_5 to D_{14}) has been selected to represent different detection conditions (Table III). The scenarios are grouped into two categories. Direct deviation cases present observable shifts in one or more sensor channels and serve as a baseline for detection. Topologically complex cases are characterized by gradual distributional changes or inter-sensor correlations, in which no single channel exhibits a dominant shift. This distinction allows examination of model behavior under different anomaly representations.

TABLE III
DESCRIPTION OF SELECTED SKAB ANOMALY SCENARIOS.

Scenario	Anomaly Description	Sensors	Max γ_s
	Direct deviation scenarios		
5	Sharp rotor imbal. behavior	ACC1, ACC2	24.9
6	Linear behavior of rotor imbal.	ACC1, ACC2	114.7
7	Step-like rotor imbal. behavior	ACC1, ACC2	97.2
8	Impulse-like rotor imbal. behavior	None	0.82
9	Exponential behavior of rotor imbal.	ACC1, ACC2	94.1
11	Sudden increase in water amount	ACC2, Thermo	2.93
	Topologically complex scenarios		
10	Slow increase in water amount	Flow Rate, Thermo	3.45
12	Draining water until cavitation	Flow Rate	44.5
13	Two-phase flow supply (cavitation)	None	1.06
14	Water supply of increased temp.	Thermocouple	3.82

C. Scenario Analysis

Scenario characterization is based on the structure of the sensor signal. A normalized mean shift is computed for each sensor s:

$$\gamma_s = \frac{|\bar{x}_{\text{anom}}(s) - \bar{x}_{\text{norm}}(s)|}{\text{std}_{\text{norm}}(s)} \tag{8}$$

This metric captures the mean displacement per channel. Low γ_s values indicate anomalies characterized through distributional shape or inter-sensor correlations rather than mean shifts.

Direct deviation scenarios. Scenarios 5, 6, 7, and 9 show large accelerometer signal shifts, with $\gamma_s > 20$ in Scenario 5 and $\gamma_s > 80$ in Scenarios 7 and 9. Scenario 8 presents an impulse pattern with $\gamma_s < 1$, where detection depends on distributional shape. Scenario 11 exhibits a weak multivariate shift across ACC2 ($\gamma_s = 2.93$) and Thermocouple ($\gamma_s = 1.21$).

Topologically complex scenarios. Scenario 10 shows gradual variation in Flow Rate ($\gamma_s = 3.45$) and Thermocouple ($\gamma_s = 1.84$). Scenario 12 presents a strong shift in Flow Rate ($\gamma_s = 44.5$), concentrated in the final phase. Scenario 13 has no dominant signal ($\gamma_s < 1.1$), and the anomaly appears only in multivariate correlations. Scenario 14 represents a thermal gradient, with Thermocouple at $\gamma_s = 3.82$ and fluid temperature at $\gamma_s = 0.69$. Table III summarizes the sensors used and the maximum γ_s for all scenarios.

D. Data-Centric Benchmarking Protocol

The data-centric benchmarking protocol is presented in Fig. 1. The workflow includes classical preprocessing and dimensionality reduction, followed by quantum feature mapping, kernel estimation via qIT and one-class optimization. The same pipeline is applied to all models to isolate the effect of kernel representation. A unified one-class setting is defined. Training uses only nominal samples, without anomaly labels. For each scenario $D_i \in \{D_5, \ldots, D_{14}\}$, the first anomaly timestamp t_{fault} is identified. A training window of $n_{\text{train}} = 240$ nominal samples is extracted before the fault. A test window

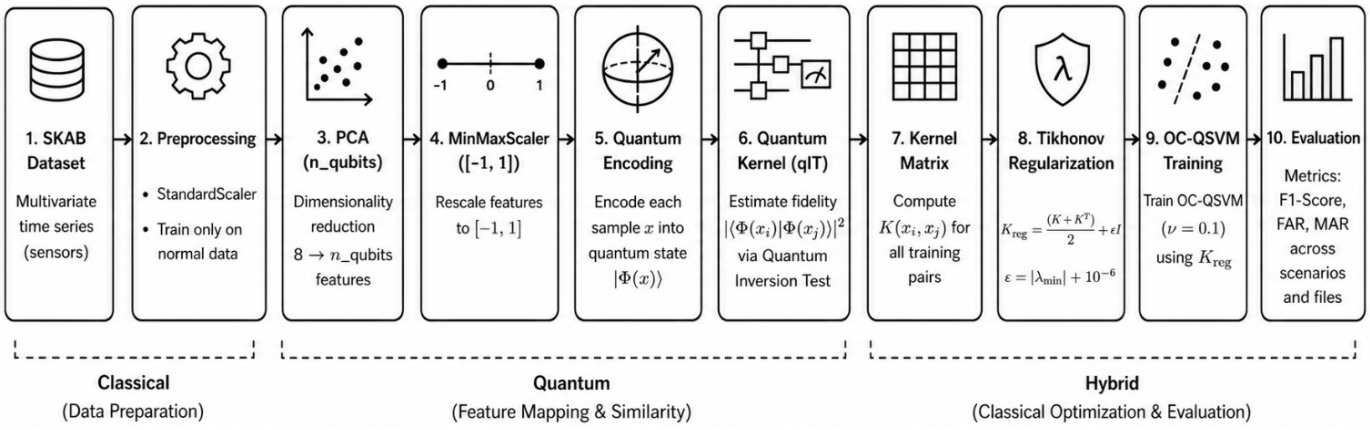

Fig. 1. Data-centric workflow for OC-QSVM with qIT kernel. The pipeline includes (i) classical preprocessing and dimensionality reduction, (ii) quantum feature mapping and kernel estimation via qIT, and (iii) hybrid optimization including evaluation.

of $n_{\text{test}} = 60$ samples is centered around t_{fault}, with anomaly proportion $n_{\text{anom}} = \text{round}(n_{\text{test}} \times r_i)$, where r_i is scenario dependent. The same partition is used across all models. Preprocessing is shared across methods. A `StandardScaler` is fitted on the training data and applied to both splits. `PCA` reduces the eight sensor channels to four components. For the qIT kernel, a `MinMaxScaler` maps inputs to $[-1, 1]$ following [28]. Reconstruction models use temporal sequences derived from normalized data. Data leakage is avoided. Six models are evaluated under this protocol. The OC-QSVM with qIT kernel is the proposed method. The OC-SVM with RBF kernel is used as the classical counterpart [24]. Additional baselines include Conv-AE, MSCRED, LSTM-AE and Isolation Forest. Performance is evaluated using F1 Score, False Alarm Rate (FAR) and Missed Alarm Rate (MAR) [8], [13], [30], [35]. Metrics are computed on the test data partition only. The protocol is reproducible with code and data available online[1].

E. Quantum Circuit Implementation

Quantum computations are executed using `AerSimulator` from `qiskit-aer` (Qiskit 1.x) on high-performance NVIDIA cuQuantum hardware equipped with NVIDIA GPU 5090 (32 GB GDDR7 memory). No physical native quantum device is used, so hardware noise sources are not present. Results are therefore free from gate errors, decoherence issues and crosstalk noise present in current devices. A shared preprocessing pipeline is used across all models. Data are standardized, reduced from eight SKAB sensor channels to four components via PCA and scaled to $[-1, 1]$ for quantum encoding downstream. The four components are mapped to four qubits. Data encoding is performed through a parameterized feature map. Each layer applies Hadamard gates, followed by single qubit $R_z(x_i)$ rotations and pairwise $R_{zz}(x_i \cdot x_j)$ interactions. Three re-upload repetitions define a six-layer circuit across four qubits.

[1]https://github.com/QuantumC3-FURG/oc-qsvm-benchmark

Kernel similarity is estimated using the Quantum Inversion Test (qIT) [28]. Each entry is computed as $K(x_1, x_2) = P(|0 \cdots 0\rangle)$ after applying $U(x_1)U(x_2)^\dagger$, with $n_{\text{shots}} = 1000$. The resulting matrix is used as a precomputed kernel in the OC-SVM solver. Finite shots introduce noise of order $1/\sqrt{n_{\text{shots}}}$, which may affect matrix definiteness. Tikhonov regularization is applied, $K_{\text{reg}} = (K + K^\top)/2 + \varepsilon I$, with $\varepsilon = |\lambda_{\min}| + 10^{-6}$, to stabilize optimization. Kernel matrices are cached across seeds to reduce computation. Each entry is indexed by a composite seed. Average execution time is approximately 2200 seconds per dataset file and seed under the base configuration. This computational cost limits scalability in current implementations.

F. Baseline Methods

The following baseline methods are included in the data-centric benchmarking protocol. They are unsupervised models used for comparison under the same evaluation conditions.

Convolutional Autoencoder (Conv-AE): Conv-AE is used to model spatial and nonlinear dependencies in multivariate data. The encoder compresses inputs into a latent representation and the decoder reconstructs the data to the original space. Anomalies are identified using reconstruction error: higher values indicate deviations from learned normal patterns [44]. This formulation is the basis for reconstruction-based detection in deep learning architectures.

Multi Scale Convolutional Recurrent Encoder Decoder (MSCRED): MSCRED models multivariate time series using ConvLSTM layers and attention mechanisms. A signature matrix is constructed from pairwise interactions among variables, capturing magnitude and interdependence. Anomalies are detected through reconstruction error on these matrices [45]. This approach shifts the focus from individual signals to their covariance structure.

Long Short Term Memory Autoencoder (LSTM-AE): LSTM-AE extends reconstruction-based detection to sequential data. The encoder compresses temporal patterns into a latent vector, and the decoder reconstructs the sequence.

Anomalies are identified when reconstruction error exceeds a threshold [46], [47]. This approach extends reconstruction-based detection to temporal dynamics.

Isolation Forest (IForest): Isolation Forest detects anomalies by recursively partitioning the feature space at random. Samples that require fewer splits to be isolated are assigned higher anomaly scores. The method assumes that anomalies are rare and distinct from normal instances. These samples are isolated with fewer partitioning steps. This approach differs from reconstruction-based models in that it relies on partitioning behavior [48].

IV. Experimental Results and Discussion

The experimental design used the chosen subset of SKAB scenarios, each treated as an independent dataset (Table III). A factorial design was defined across 6 models and 10 anomaly scenarios. Each experiment was repeated five times to account for inter-experimental variability. A one-way ANOVA was calculated across repetitions, with a p-value consistently above 0.05. This confirmed that there was no statistically significant variation across runs.

Aggregate results in Fig. 2 show that Conv-AE achieves the highest mean F1 (0.744), whereas OC-SVM and OC-QSVM obtain 0.670 and 0.629, respectively. Isolation Forest presents the highest FAR (0.810), whereas Conv-AE shows the lowest (0.010). LSTM-AE produces the highest MAR (0.603). Although it does not achieve the highest mean F1, the proposed OC-QSVM maintains a balanced trade-off between FAR (0.330) and MAR (0.249). In contrast, reconstruction-based models exhibit low FAR values but high MAR, which suggests a failure to detect anomalies in some scenarios. Isolation Forest shows the opposite behavior: low MAR (0.045) but very high FAR. This pattern reflects a stable detection regime for OC-QSVM, where both false alarms and missed anomalies remain bounded across scenarios. Such behavior is consistent with the one-class formulation under a low-data regime and aligns with the data-centric protocol defined in Section III. A low FAR associated with a high MAR corresponds to a degenerate condition in which no anomalies are predicted. This effect is observed in reconstruction-based models under topologically complex scenarios. This effect motivates the scenario-level analysis that follows.

A. Performance in Direct Deviation Scenarios

In direct deviation scenarios, detection behavior follows the magnitude of the normalized mean shift γ_s (Table III). Scenarios 6, 7 and 9 present large accelerometer displacements ($\gamma_s > 94$), and all model families achieve high F1 values (Table IV). In this regime, OC-QSVM achieves 0.898, 0.751 and 0.699, which remain close to OC-SVM and are lower than those of reconstruction-based models. This pattern reflects that strong mean shifts reduce the impact of the kernel representation. A different behavior appears in moderate and distributed cases. In Scenario 5 ($\gamma_s = 24.9$), OC-QSVM achieves F1 $= 0.705$, below Conv-AE (0.976) but above Isolation Forest (0.532). In Scenario 11, where the anomaly is distributed across channels (ACC2 and Thermocouple), OC-QSVM reaches F1 $= 0.667$, whereas Conv-AE achieves 0.930. However, reconstruction-based models maintain near-zero FAR in these scenarios, albeit at the cost of higher MAR. This may suggest a selective detection.

The most distinct behavior appears in Scenario 8, where $\gamma_s < 1$ and no dominant mean shift is present. Reconstruction-based models achieve high F1 (Conv-AE 0.976 and MSCRED 0.950). OC-QSVM achieves an F1 score of 0.460 in this scenario. In this case, the anomaly is a short impulse; detection depends on the transient distributional shape. The one-class boundary defined by OC-QSVM does not capture this structure effectively within the given sample window. Across direct deviation scenarios, OC-QSVM maintains bounded FAR and MAR values without degeneracy. In Scenarios 5–9 and 11, MAR remains below 0.13 except for the impulse case. Also, FAR values remain within a controlled range. In contrast, Isolation Forest consistently yields high FAR (up to 1.000), whereas reconstruction-based models achieve low FAR but exhibit variable MAR. This behavior suggests that OC-QSVM provides stable detection across varying mean-shift conditions. Although it does not achieve the highest F1 score in dominant-shift scenarios, it keeps a consistent balance between false alarms and missed detections across all cases. This property becomes more relevant when anomaly structure departs from a single-sensor data channel, as explored in the following subsection.

B. Performance in Topologically Complex Scenarios

Topologically complex scenarios reveal a different detection behavior. Reconstruction-based models show a degenerate classification pattern (F1 $= 0.00$, FAR $= 0.000$ and MAR $= 1.000$), which results in no anomaly detection. This behavior is present in Scenario 10 for all reconstruction models and in Scenario 14 for Conv-AE and LSTM-AE. The anomaly signal does not shift the reconstruction error distribution beyond the learned threshold under limited nominal training. Scenario 10 is the most discriminating case in this benchmarking dataset. As shown in Fig. 3, the anomaly corresponds to a slow increase in water amount in which the flow-rate declines gradually through the anomaly segment. No accelerometer shift is observed ($\gamma_s = 3.45$ on flow rate only), and reconstruction error thresholds calibrated on nominal data remain insensitive to the drift. In this setting, OC-QSVM achieves F1 $= 0.733$, the highest among all models, with FAR $= 0.141$. Isolation Forest reaches a similar F1 (0.725) but with much higher FAR (0.529). OC-SVM achieves F1 $= 0.700$ with zero FAR but high MAR (0.462). Only kernel-based models maintain active detection in such a complex scenario. In Scenario 14, OC-QSVM achieves F1 $= 0.359$, exceeding reconstruction models that produce no detections, while remaining below Isolation Forest and MSCRED. Scenario 12 shows a large mean shift ($\gamma_s = 44.5$), but detection remains limited. OC-QSVM achieves F1 $= 0.314$ with high FAR (0.848), as the test window captures intermediate states before the dominant signal change [23].

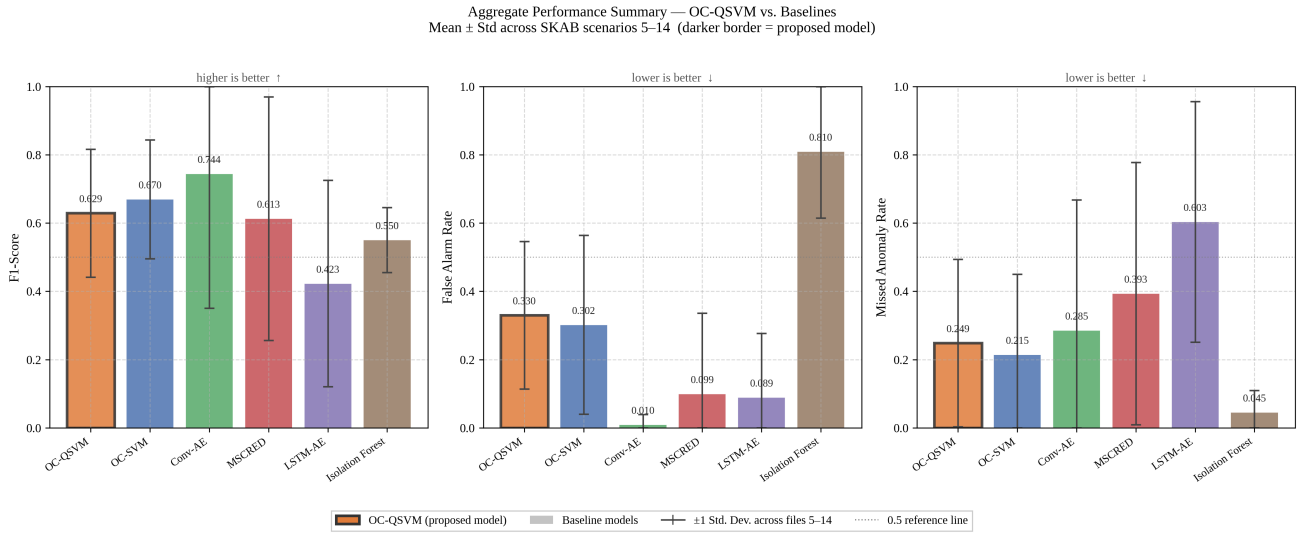

Fig. 2. Aggregate performance across scenarios 5–14. Mean ± one standard deviation across data files is reported for F1 Score (higher is better), FAR (lower is better) and MAR (lower is better). The OC-QSVM is presented through a darker border.

TABLE IV

FULL BENCHMARK RESULTS ACROSS SKAB SCENARIOS 5–14. F1-SCORE (↑), FAR (↓), AND MAR (↓) ARE REPORTED. **BOLD** DENOTES THE BEST RESULT FOR EACH SCENARIO. OC-QSVM† VALUES ARE AVERAGED OVER FIVE RANDOM SEEDS USING THE QIT KERNEL ON AERSIMULATOR.

	Direct Deviation Scenarios						*Topologically Complex Scenarios*			
Scenario	**5**	**6**	**7**	**8**	**9**	**11**	**10**	**12**	**13**	**14**
					F1-Score ↑					
OC-QSVM†	0.705	0.898	0.751	0.460	0.699	0.667	**0.733**	0.314	0.704	0.359
OC-SVM	0.750	0.913	0.766	0.474	0.690	0.742	0.700	0.299	0.769	0.595
Conv-AE	**0.976**	0.923	**0.944**	**0.976**	**0.923**	**0.930**	0.000	**0.900**	**0.867**	0.000
MSCRED	0.592	**0.950**	0.783	0.950	0.865	0.606	0.000	0.000	**0.867**	0.519
LSTM-AE	0.727	0.727	0.643	0.091	0.700	0.296	0.000	0.588	0.455	0.000
Isolation Forest	0.532	0.609	0.581	0.522	0.519	0.543	0.725	0.462	0.378	**0.635**
					False Alarm Rate (FAR) ↓					
OC-QSVM†	0.451	0.123	0.268	0.215	0.359	0.459	0.141	0.848	0.205	0.230
OC-SVM	0.359	0.103	0.244	0.205	0.436	0.432	**0.000**	0.929	0.163	0.150
Conv-AE	**0.000**	**0.000**	**0.000**	**0.000**	**0.000**	**0.000**	**0.000**	0.095	**0.000**	**0.000**
MSCRED	0.744	**0.000**	0.220	**0.000**	**0.000**	**0.000**	0.029	**0.000**	**0.000**	**0.000**
LSTM-AE	**0.000**	**0.000**	**0.000**	**0.000**	0.462	**0.000**	**0.000**	0.429	**0.000**	**0.000**
Isolation Forest	0.949	0.692	0.610	0.769	1.000	0.973	0.529	1.000	1.000	0.575
					Missed Alarm Rate (MAR) ↓					
OC-QSVM†	**0.000**	**0.000**	**0.053**	0.581	0.105	0.130	0.315	0.444	0.176	0.680
OC-SVM	**0.000**	**0.000**	**0.053**	0.571	0.048	**0.000**	0.462	0.444	**0.118**	0.450
Conv-AE	0.048	0.143	0.105	**0.048**	0.143	0.130	1.000	**0.000**	0.235	1.000
MSCRED	**0.000**	0.095	**0.053**	0.095	0.238	0.565	1.000	1.000	0.235	0.650
LSTM-AE	0.429	0.429	0.526	0.952	**0.000**	0.826	1.000	0.167	0.706	1.000
Isolation Forest	**0.000**	**0.000**	**0.053**	0.143	**0.000**	0.044	**0.038**	**0.000**	0.177	**0.000**

† OC-QSVM: mean over five seeds; qIT kernel with $n_{\text{shots}} = 1000$ on `AerSimulator` (Qiskit 1.x); PCA to 4 components.

In complex scenarios, OC-QSVM maintains non-degenerate detection while keeping FAR and MAR bounded. This behavior is not observed in reconstruction-based models, which collapse to MAR $= 1.0$ in the same scenarios, thus failing under anomaly data distributed across multiple variables. The results suggest that kernel-based representations remain responsive when anomalies are not separable through single-sensor statistics. A consistent advantage for the quantum model cannot be established from these results. However, improved performance in selected topologically complex scenarios suggests a

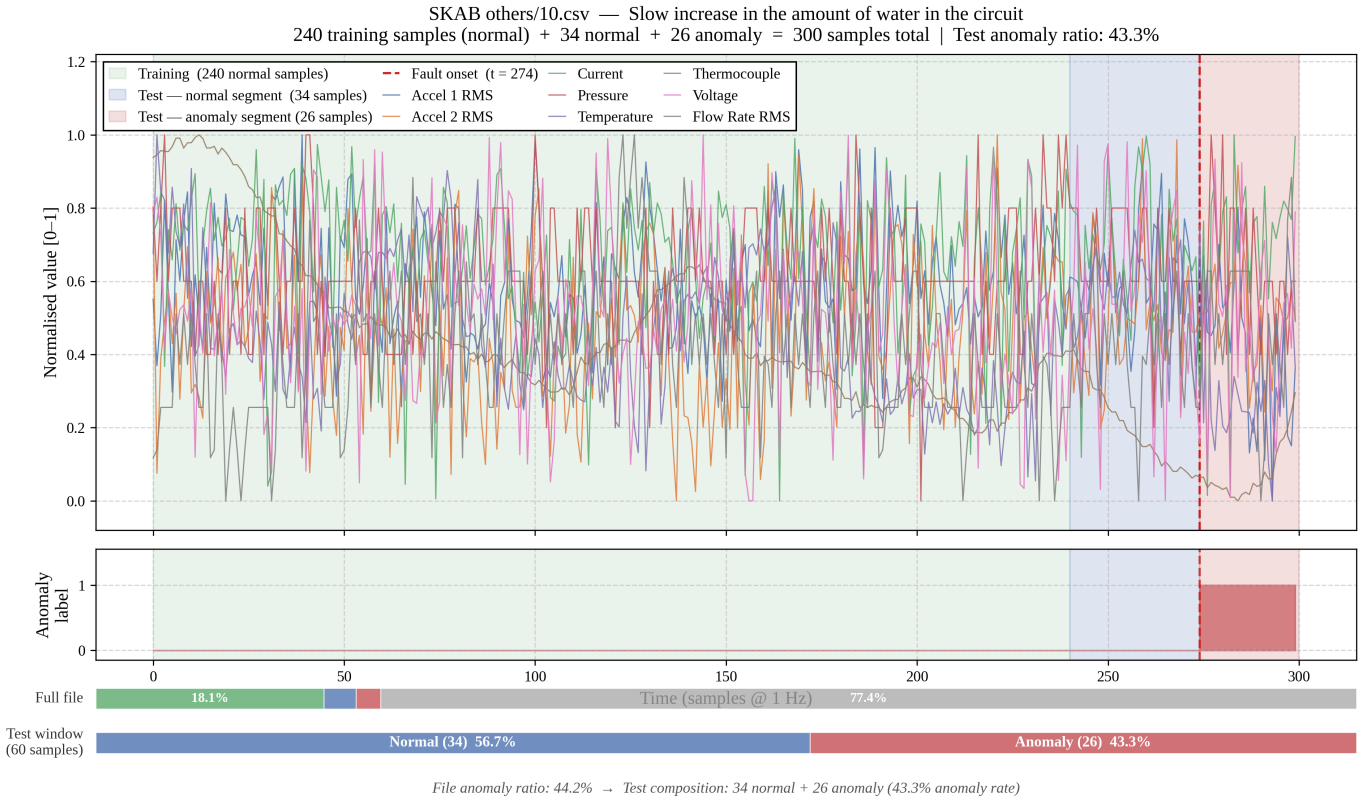

Fig. 3. Data partitioning for Scenario 10 (slow increase in water volume). The flow rate declines gradually across the anomaly segment, without producing a shift detectable by reconstruction-error thresholds. Training uses 240 nominal samples preceding the test window.

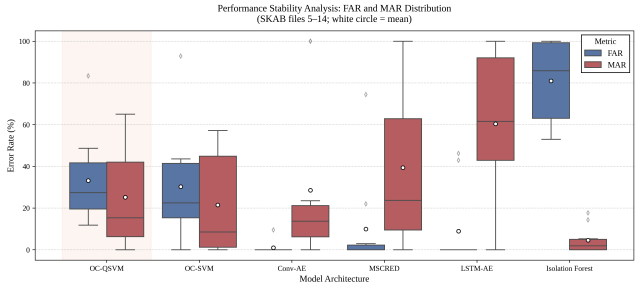

Fig. 4. FAR and MAR distributions across scenarios 5–14. White circles indicate the mean. Reconstruction-based models exhibit wide MAR distributions, with LSTM-AE and MSCRED reaching values of 100% in complex scenarios.

possible benefit when anomalies depend on multivariate data. This effect may be related to the representation induced in Hilbert space, which remains to be examined in future work.

C. Error Distributions and Stability

FAR and MAR distributions in Fig. 4 differ across model families. The stability of OC-QSVM across seeds is reported in Table V. LSTM-AE and MSCRED show wide MAR data distributions (reaching 100%). Conv-AE keeps a low FAR but produces a MAR outlier at 100% in Scenario 10. Isolation Forest exhibits a low MAR, with consistently high FAR across all scenarios. The relative F1 analysis in Fig. 5 suggests that OC-QSVM does not produce the worst result in any scenario. In contrast, Conv-AE, MSCRED and LSTM-AE reach worst-case results in at least one scenario. Isolation Forest reaches FAR $= 1.000$ in Scenarios 9 and 12. Kernel-based models maintain bounded error distributions across all cases [3], [28]. OC-QSVM presents a higher median FAR ($\approx 29\%$) than OC-SVM ($\approx 23\%$), which may suggest a higher rate of false positives under the qIT kernel in the one-class regime.

V. Conclusions

An unsupervised learning method, named OC-QSVM, was introduced for one-class anomaly detection using a quantum kernel based on the quantum inversion test. The method was evaluated within a data-centric benchmarking protocol, in which six unsupervised models were compared under identical conditions across 10 SKAB scenarios. Training was restricted to nominal data, which isolates the effect of kernel representation in a low-data regime.

The research question investigated to what extent replacing an RBF kernel with a quantum kernel affects the error distribution in a low-data regime and under varying anomaly structures. The results show that the effect depends on scenario type. In cases of direct deviation, both kernels achieved similar F1 scores. In topologically complex scenarios, reconstruction-based models have not fully succeeded in multiple cases

TABLE V
OC-QSVM STABILITY ACROSS FIVE RANDOM SEEDS. MEAN ± STANDARD DEVIATION IS REPORTED FOR F1-SCORE, FAR AND MAR ACROSS SCENARIOS.

Scenario	F1 ↑	FAR ↓	MAR ↓
Direct Deviation Scenarios			
5	0.705 ± 0.010	0.451 ± 0.023	0.000 ± 0.000
6	0.898 ± 0.009	0.123 ± 0.011	0.000 ± 0.000
7	0.751 ± 0.025	0.268 ± 0.039	0.053 ± 0.000
8	0.460 ± 0.036	0.215 ± 0.014	0.581 ± 0.040
9	0.699 ± 0.011	0.359 ± 0.000	0.105 ± 0.021
11	0.667 ± 0.008	0.459 ± 0.019	0.000 ± 0.000
Topologically Complex Scenarios			
10	0.733 ± 0.012	0.141 ± 0.025	0.315 ± 0.017
12	0.314 ± 0.003	0.848 ± 0.013	0.444 ± 0.000
13	0.704 ± 0.015	0.205 ± 0.019	0.176 ± 0.000
14	0.359 ± 0.023	0.230 ± 0.011	0.680 ± 0.027
Mean std	*0.015*	*0.017*	*0.011*

with MAR $= 1.000$, while both kernel methods maintained detection. The OC-QSVM achieved the highest F1 Score in Scenario 10 (0.733), which is considered the most discriminative case in the benchmark.

Across all scenarios, the OC-QSVM maintained bounded FAR and MAR and did not produce the worst result in any metric. Scenario-level evaluation showed stable behavior under both dominant and distributed anomaly structures. The OC-SVM achieved lower median FAR ($\approx 23\%$ vs $\approx 29\%$) with comparable F1. No consistent advantage in aggregate F1 was observed for the quantum model. However, improved performance in selected complex scenarios suggests a potential benefit when anomalies depend on multivariate time series structure.

The results are limited to simulation and a fixed feature map. Future work will evaluate quantum hardware and alternative encodings and extend the protocol to broader datasets to further examine this effect.

ACKNOWLEDGMENT

This work was supported by CAPES (Brazil) and the PRH-ANP program, managed by FAPESP under process 2025/03736-5. *Disclosure of AI Usage:* Google NotebookLM (premium version) was used for text summarization and Grammarly was used for grammar revision. All outputs were reviewed and selectively integrated. The final text reflects the author's own understanding and complies with IEEE and institutional academic integrity policies.

REFERENCES

[1] A. I. Jawad, E. Stefan-Henningsen, and A. Kiani, "Applications of classical and quantum machine learning in manufacturing: Predictive maintenance, scheduling and tribology," *Next Research*, 2026.

[2] S. Badami, "Hardware-agnostic quantum kernel feature mapping for anomaly detection in critical infrastructure: A cross-testbed validation on nisq processors," *IEEE Access*, vol. 14, pp. 49 642–49 654, 2026.

[3] T. Cultice, M. S. H. Onim, A. Giani, and H. Thapliyal, "Quantum-hybrid support vector machines for anomaly detection in industrial control systems," *ArXiv*, vol. abs/2506.17824, 2025.

[4] K. Sudharson, S. Varsha, R. Santhiya, and D. Rajalakshmi, "Quantum-enhanced lstm for predictive maintenance in industrial iot systems," *MethodsX*, vol. 15, 2025.

[5] A. Diedrich, S. Windmann, and O. Niggemann, "Solving industrial fault diagnosis problems with quantum computers," *Quantum Machine Intelligence*, vol. 6, 2024.

[6] F. Li, W. Xiang, J. Wang, X. Zhou, and B. Tang, "Quantum weighted long short-term memory neural network and its application in state degradation trend prediction of rotating machinery," *Neural networks : the official journal of the International Neural Network Society*, vol. 106, pp. 237–248, 2018.

[7] J. Stein, M. Poppel, P. Adamczyk, R. Fabry, Z.-X. Wu, M. Kölle, J. Nüßlein, D. Schuman, P. Altmann, T. Ehmer, V. Narasimhan, and C. Linnhoff-Popien, "Benchmarking quantum surrogate models on scarce and noisy data," in *International Conference on Agents and Artificial Intelligence*, 2023.

[8] C. Zhang, D. Song, Y. Chen, X. Feng, C. Lumezanu, W. Cheng, J. Ni, B. Zong, H. Chen, and N. V. Chawla, "A deep neural network for unsupervised anomaly detection and diagnosis in multivariate time series data," in *Proceedings of the AAAI conference on artificial intelligence*, vol. 33, no. 01, 2019, pp. 1409–1416.

[9] E. Choi, J. Sul, J. E. Kim, S. J. Hong, B. I. Gonzalez, P. Cembellin, and Y. Wang, "Quantum machine learning for additive manufacturing process monitoring," *Manufacturing Letters*, 2024.

[10] K. Tscharke, S. Issel, and P. Debus, "Semisupervised anomaly detection using support vector regression with quantum kernel," *2023 IEEE International Conference on Quantum Computing and Engineering (QCE)*, vol. 01, pp. 611–620, 2023.

[11] C. Correa-Jullian, S. Cofre-Martel, G. S. Martín, E. L. Droguett, G. de Novaes Pires Leite, and A. B. R. Costa, "Exploring quantum machine learning and feature reduction techniques for wind turbine pitch fault detection," *Energies*, 2022.

[12] B. Krishnamurthy, S. Das, and S. G. Shiva, "Early detection of virtual machine failures in cloud computing using quantum-enhanced support vector machine," *Mathematics*, 2026.

[13] D. Lee, H. Choo, and J. W. Jeong, "Anomaly detection based on 1d-cnn-lstm auto-encoder for bearing data," *WSEAS TRANSACTIONS ON INFORMATION SCIENCE AND APPLICATIONS*, 2023.

[14] M. Incudini, D. L. Bosco, F. D. Martini, M. Grossi, G. Serra, and A. D. Pierro, "Automatic and effective discovery of quantum kernels," *IEEE Transactions on Emerging Topics in Computational Intelligence*, 2022.

[15] S. Tomar, R. Tripathi, and S. Kumar, "Comprehensive survey of qml: From data analysis to algorithmic advancements," *ArXiv*, vol. abs/2501.09528, 2025.

[16] J. eun Park, B. Quanz, S. P. Wood, H. Higgins, and R. Harishankar, "Practical application improvement to quantum svm: theory to practice," *ArXiv*, vol. abs/2012.07725, 2020.

[17] U. Singh, J. F. 'ed 'eric Laprade, A. Z. Goldberg, and K. Heshami, "A resource efficient quantum kernel," *ArXiv*, vol. abs/2507.03689, 2025.

[18] Y.-Y. Hong and D. J. D. Lopez, "A review on quantum machine learning in applied systems and engineering," *IEEE Access*, vol. 13, pp. 144 607–144 631, 2025.

[19] S. Ill'esov'a, T. Rybotycki, and M. Beseda, "Qmetric: Benchmarking quantum neural networks across circuits, features, and training dimensions," 2025.

[20] J. Tian and W. Yang, "Explainable quantum neural networks: Example-based and feature-based methods," *Electronics*, 2024.

[21] F. Rodríguez-Díaz, D. Gutiérrez-Avilés, A. Troncoso, and F. Martínez-Álvarez, "A survey of quantum machine learning: Foundations, algorithms, frameworks, data and applications," *ACM Computing Surveys*, 2025.

[22] J. J. Park, J. Cha, S. Y.-C. Chen, H.-H. Tseng, and S. Yoo, "Addressing the current challenges of quantum machine learning through multi-chip ensembles," *ArXiv*, vol. abs/2505.08782, 2025.

[23] I. D. Katser and V. O. Kozitsin, "Skoltech anomaly benchmark (skab)," https://www.kaggle.com/dsv/1693952, 2020.

[24] B. Scholkopf, R. C. Williamson, A. Smola, J. Shawe-Taylor, and J. C. Platt, "Support vector method for novelty detection," in *Neural Information Processing Systems*, 1999.

[25] O. Schütt and J. VandeVondele, "Machine learning adaptive basis sets for efficient large scale density functional theory simulation," *Journal of Chemical Theory and Computation*, vol. 14, pp. 4168 – 4175, 2018.

[26] G. Park, J. Huh, and D. K. Park, "Variational quantum one-class classifier," *Machine Learning: Science and Technology*, vol. 4, 2022.

[27] M. Hdaib, S. Rajasegarar, and L. Pan, "Quantum deep learning-based anomaly detection for enhanced network security," *Quantum Machine Intelligence*, vol. 6, 2024.

[28] M. Kölle, A. Ahouzi, P. Debus, R. Müller, D. Schuman, and C. Linnhoff-Popien, "Towards efficient quantum anomaly detection: One-class svms using variable subsampling and randomized measurements," *ArXiv*, vol. abs/2312.09174, 2023.

[29] M. Kölle, A. Ahouzi, P. Debus, E. Çetiner, R. Müller, D. Schuman, and C. Linnhoff-Popien, "Efficient quantum one-class support vector machines for anomaly detection using randomized measurements and variable subsampling," *ArXiv*, vol. abs/2407.20753, 2024.

[30] S. K. Jasra, G. Valentino, A. Muscat, and R. Camilleri, "A comparative study of unsupervised deep learning methods for anomaly detection in flight data," *Aerospace*, 2025.

[31] M. A. Alam and S. Ghosh, "Deepqmlp: A scalable quantum-classical hybrid deep neural network architecture for classification," *2022 35th International Conference on VLSI Design and 2022 21st International Conference on Embedded Systems (VLSID)*, pp. 275–280, 2022.

[32] E. S. Teixeira, Y. Inácio, and P. T. L. Bezerra, "Applying quantum tensor networks in machine learning: A systematic literature review," in *International Conference on Agents and Artificial Intelligence*, 2025.

[33] D. Ranga, A. Rana, S. Prajapat, P. Kumar, K. Kumar, and A. V. Vasilakos, "Quantum machine learning: Exploring the role of data encoding techniques, challenges, and future directions," *Mathematics*, 2024.

[34] C. Pere, "Data complexity: a threshold between classical and quantum machine learning – part i," 2025.

[35] A. Ghosh, S. Dutta, A. K. Das, V. K. Shukla, and F. Moreira, "Quantum machine learning in industrial automation," *Quantum Machine Learning in Industrial Automation*, 2025.

[36] J. Cunningham and J. Zhuang, "Investigating and mitigating barren plateaus in variational quantum circuits: a survey," *Quantum Information Processing*, vol. 24, no. 2, p. 48, Jan 2025.

[37] J. R. McClean, S. Boixo, V. N. Smelyanskiy, R. Babbush, and H. Neven, "Barren plateaus in quantum neural network training landscapes," *Nature Communications*, vol. 9, no. 1, p. 4812, Nov 2018.

[38] J. Schnabel and M. Roth, "Quantum kernel methods under scrutiny: a benchmarking study," *Quantum Machine Intelligence*, vol. 7, 2024.

[39] M. Schuld, "Supervised quantum machine learning models are kernel methods," 2021. [Online]. Available: https://arxiv.org/abs/2101.11020

[40] K. Muandet and B. Scholkopf, "One-class support measure machines for group anomaly detection," *ArXiv*, vol. abs/1303.0309, 2013.

[41] X. Wang, Y. Du, Y. Luo, and D. Tao, "Towards understanding the power of quantum kernels in the nisq era," *Quantum*, vol. 5, p. 531, 2021.

[42] H. Thompson-Bahm, J. E. Teixeira, and R. C. G. Lobo, "Enhancing sustainability and human centricity through emerging technologies from industry 4.0 to industry 5.0: An integrative literature review," *Corporate Governance and Sustainability Review*, 2025.

[43] J. Alves, T. M. Lima, and P. D. Gaspar, "Is industry 5.0 a human-centred approach? a systematic review," *Processes*, 2023.

[44] D. M. Hibban and K. Surendro, "Unsupervised anomaly detection in hospital wastewater effluent using convolutional autoencoder," *Journal of Information Systems Engineering and Business Intelligence*, 2026.

[45] Z. Chen, M. Wang, J. Li, G. Li, and X. Wu, "Unsupervised anomaly detection methods for in situ observation data: A comparative study," *IEEE Access*, vol. 13, pp. 187 347–187 360, 2025.

[46] Z. Wang, M. K. Dahouda, H. Hwang, and I. Joe, "Explanatory lstm-ae-based anomaly detection for time series data in marine transportation," *IEEE Access*, vol. 13, pp. 23 195–23 208, 2025.

[47] G. Park and J. Kim, "Multivariate variable-based lstm-ae model for solar power prediction," *International Journal on Advanced Science, Engineering and Information Technology*, 2025.

[48] M. Saremi, A. Hezarkhani, S. A. A. S. Mirzabozorg, R. DehghanNiri, A. Shirazy, and A. Shirazi, "Unsupervised anomaly detection for mineral prospectivity mapping using isolation forest and extended isolation forest algorithms," *Minerals*, 2025.

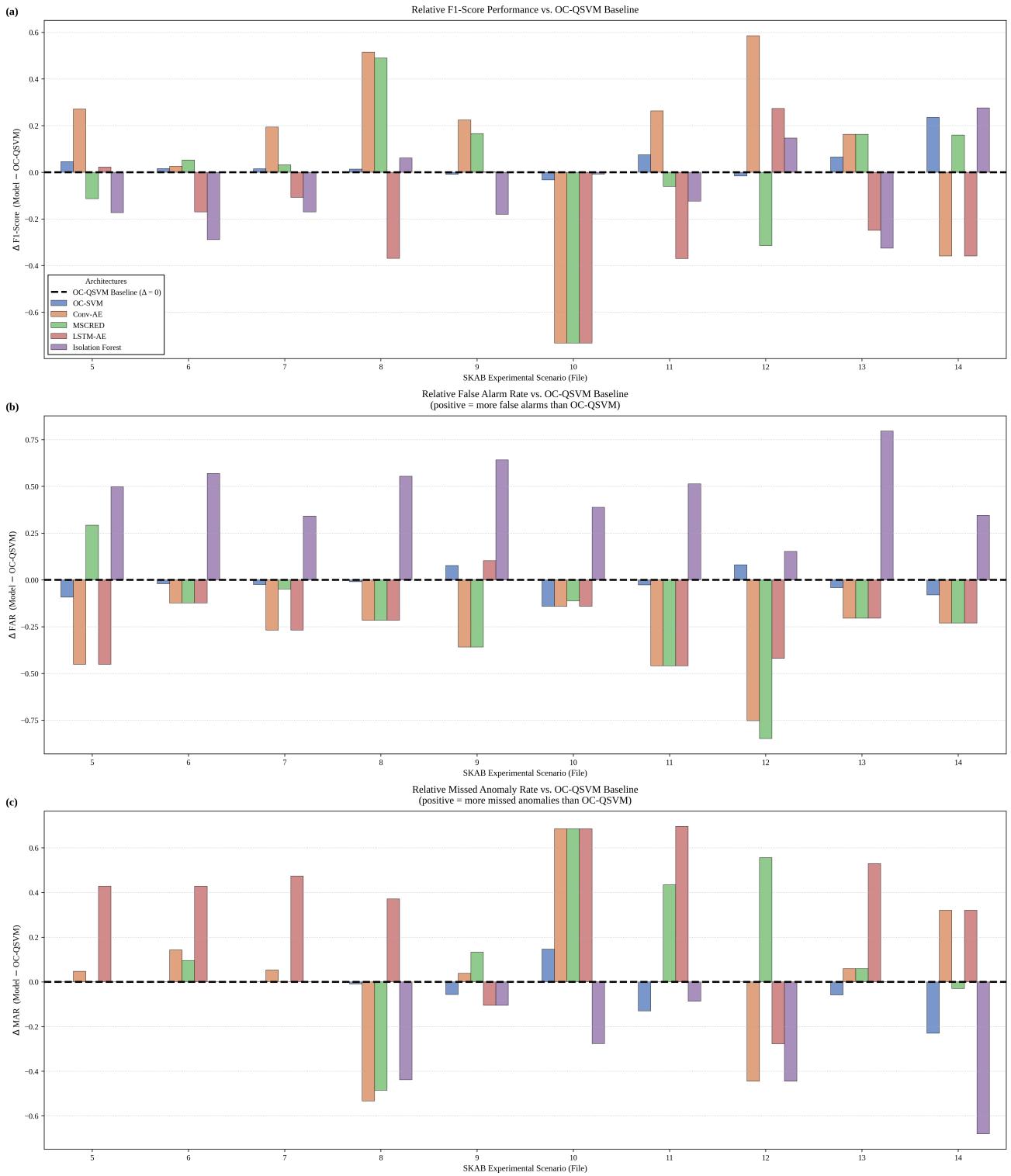

Fig. 5. Relative performance across SKAB scenarios 5–14 for (a) F1-Score, (b) False Alarm Rate (FAR), and (c) Missed Alarm Rate (MAR). The OC-QSVM baseline is indicated by a dashed line ($\Delta = 0$). Positive values correspond to higher values than the baseline. Negative values correspond to lower values.